

Dynamical difference between the cD galaxy and the diffuse, stellar component in simulated galaxy clusters

K. Dolag^{1*}, G. Murante² and S. Borgani^{3,4,5}

¹ *Max-Planck-Institut für Astrophysik, Karl-Schwarzschild Strasse 1, Garching bei München, Germany (kdolag@mpa-garching.mpg.de)*

² *INAF – Astronomical Observatory of Torino, Str. Osservatorio 25, I-10025, Pino Torinese, Torino, Italy*

³ *Dipartimento di Astronomia dell'Università di Trieste, via Tiepolo 11, I-34131 Trieste, Italy (borgani@oats.inaf.it)*

⁴ *INFN – Istituto Nazionale di Fisica Nucleare, Trieste, Italy*

⁵ *INAF – Istituto Nazionale di Astrofisica, Trieste, Italy*

Accepted ???. Received ???; in original form ???

ABSTRACT

Member galaxies within galaxy clusters nowadays can be routinely identified in cosmological, hydrodynamical simulations using methods based on identifying self bound, locally over dense substructures. However, distinguishing the central galaxy from the stellar diffuse component within clusters is notoriously difficult, and in the center it is not even clear if two distinct stellar populations exist. Here, after subtracting all member galaxies, we use the velocity distribution of the remaining stars and detect two dynamically, well-distinct stellar components within simulated galaxy clusters. These differences in the dynamics can be used to apply an un-binding procedure which leads to a spatial separation of the two components into a cD and a diffuse stellar component (DSC). Applying our new algorithm to a cosmological, hydrodynamical simulation we find that – in line with previous studies – these two components have clearly distinguished spatial and velocity distributions as well as different star formation histories. We show that the DSC fraction – which can broadly be associated with the observed intra cluster light – does not depend on the virial mass of the galaxy cluster and is much more sensitive to the formation history of the cluster. We conclude that the separation of the cD and the DSC in simulations, based on our dynamical criteria, is more physically motivated than current methods which depend on implicit assumptions on a length scale associated with the cD galaxy and therefore represent a step forward in understanding the different stellar components within galaxy clusters. Our results also show the importance of analyzing the dynamics of the DSC to characterize its properties and understand its origin.

Key words: hydrodynamics, method: numerical, galaxies: cluster: general, galaxies: evolution, cosmology: theory

1 INTRODUCTION

The existence of a diffuse stellar component in groups and clusters of galaxies is now well established. A diffuse intra-cluster light (ICL) has been observed both in local universe (Feldmeier et al. 2004; Mihos et al. 2005; Arnaboldi et al. 2004; Gerhard et al. 2005; Doherty et al. 2009) and at intermediate redshift (Gonzalez et al. 2000; Feldmeier et al. 2004; Zibetti et al. 2005; Krick & Bernstein 2007). Such ICL component is centrally concentrated, and typically amounts between ≈ 10 (Zibetti et al. 2005) and ≈ 35 % (Gonzalez et al. 2007) of the total stellar mass in clusters. There are some indications pointing towards a dependence of the ICL fraction from the mass of the clusters, going from ≈ 2 % at the scale of loose groups (Castro-Rodríguez et al. 2003) to

≈ 5 – 10 % of Virgo cluster (Arnaboldi et al. 2003; Feldmeier et al. 2004; Mihos et al. 2005; Castro-Rodríguez et al. 2009) up to 10 – 20 % or higher in the most massive clusters (Gonzalez et al. 2000; Feldmeier et al. 2002; Gal-Yam et al. 2003; Feldmeier et al. 2004; Krick et al. 2006), but other studies found instead no significant dependence on the cluster richness (Zibetti et al. 2005).

ICL is usually detected using surface photometry in various bands, sometimes stacking together observations of many clusters (see e.g. Zibetti et al. 2005). In this case, light coming from galaxies is masked away, often using a fixed limit in surface brightness (e.g., as in Feldmeier et al. 2004). Single ICL stars can also be detected (Durrell et al. 2002), especially by observing Intra-Cluster Planetary Nebulae (ICPN) (Arnaboldi et al. 1996; Feldmeier et al. 2004), which can be observed up to distances as large as 100 Mpc (Gerhard et al. 2005). On the one hand, the observational effort needed to detect single stars makes it difficult to use them to as-

* E-mail: kdolag@mpa-garching.mpg.de

sess general properties of the *ICL* distribution, like the *ICL* fraction in clusters. On the other hand, the observation of single stars make it possible to gather information on the kinematic of such a component. In particular, extended halos of bright ellipticals often overlap spatially with stars which are free-floating in the cluster gravitational potential. Efforts have been made to disentangle these two components (see e.g. Doherty et al. 2009), but they are often referred together as the *ICL*. In the following, we will use *ICL* to indicate the observed diffuse stellar population, whose dynamical properties are difficult to obtain, and *DSC* for the corresponding stellar population produced in numerical simulation, whose dynamics is known.

From a theoretical point of view, a diffuse stellar component (*DSC*) has been studied in a cosmological Dark-Matter-only numerical simulation (Napolitano et al. 2003). Later, for the first time Murante et al. (2004) (M04 hereafter) studied the properties of the *DSC* in a cosmological simulation which included hydrodynamics and various astrophysical processes such as radiative cooling of gas and (self-consistent) star formation. Willman et al. (2004) and Sommer-Larsen et al. (2005) analyzed a *DSC* in their resimulation of single galaxy clusters.

M04 analyzed a cosmological simulation of a box of $192 h^{-1}$ Mpc, containing ≈ 100 galaxy cluster. Their main results were that: (i) a *DSC* is clearly seen when a Sersic fit is performed on the bound, unbound and total two-dimensional radial density profiles of the stellar population in clusters; (ii) the *DSC* component is more centrally concentrated than the stars bound in galaxies; (iii) on average, stars in the *DSC* are older than those in galaxies; (iv) the *DSC* fraction increase with the cluster mass. Willman et al. (2004) used one cluster re-simulation, having a mass of $1.2 \times 10^{15} M_{\odot}$, and confirmed results (i) of M04. They found a *DSC* fraction compatible with M04 clusters in the same mass range, if slightly lower. Sommer-Larsen et al. (2005) used one Virgo-like and one Coma-like cluster re-simulation and confirmed results (i), (ii) and (iii) of M04. They found similar *DSC* fraction, with their Coma-like cluster having an higher fraction of *DSC* stars. Their average stellar age in *DSC* was older than that found by M04.

Several mechanisms have been investigated to explain the formation and evolution of a *DSC*: stripping and disruption of galaxies as they pass through the central regions of relaxed clusters (Byrd & Valtonen 1990; Gnedin 2003); stripping of stars from galaxies during the initial formation of clusters (Merritt 1984); creation of stellar haloes in galaxy groups, that later fall into massive clusters and then become unbound (Mihos 2004; Rudick et al. 2006); and stripping of stars during high-speed galaxy encounters in the cluster environment (Moore et al. 1996). Murante et al. (2007) (M07 hereafter) showed that the *DSC* is produced during mergers in the formation history of the BCGs and of other massive galaxies, and that it grows steadily since redshift $z = 1$, with no preferred epoch of formation. Monaco et al. (2006), using a semi-analytical model of galaxy formation in clusters, showed that, in the hierarchical model of structure formation, the BCG merging activity alone between $z = 1$ and $z = 0$ is so intense that it is not possible to simultaneously fit the bright end of the galaxy luminosity function at both redshifts without assuming that a significant fraction of stars goes into the *DSC* during such mergers. Note that there are observational indications which seems to show such process in action within the Coma cluster (Gerhard et al. 2007). Numerically, Stanghellini et al. (2006) studied isolated, star-only dry merger of elliptical galaxies and showed how in that case, up to 21 % of the initial total stellar mass can become unbind in the process.

One major problem with the analysis of *DSC* in numerical

simulations is its very identification. One possibility, used e.g. by Rudick et al. (2006), is to build simulated surface brightness maps and detect an *ICL* component with a procedure similar to that used with observational data. This has the advantage of being somewhat easier to compare with observation, at the cost of losing the intrinsic advantage of simulations, that is, the knowledge of the dynamics of each star particle. The other possibility is to attempt a dynamical distinction between stars bound to galaxies and stars which are free-floating in the group or cluster potential. This is what M04, Willman et al. (2004) and Sommer-Larsen et al. (2005) did; the disadvantage is that such a distinction may or may not coincide with the observational definition of *ICL*. However, for doing this, it is necessary to identify structures in the simulation (groups or clusters) and substructures within them (the galaxies). Up to date, no unambiguous way to perform such identification has been formulated.

The identification of *structures* is a relatively easy task. The most commonly used algorithms are based upon two methods: the Friends-of-Friends (FoF) approach (Davis et al. 1985; Frenk et al. 1988) and the Spherical Overdensity one (SO) (Lacey & Cole 1994). In the former, all particles closer than a given distance l (usually expressed as fraction of the mean inter-particle distance, typically $l \approx 0.2$ is chosen) are grouped together; then, all particles closer than l to such particles are included in the group, and so on. In the latter, one identifies density peaks in the particle distribution, and puts spheres around them, choosing their radius so that they enclose a given overdensity.

The difficulty arises when *substructures* inside DM halos must be found. The density contrast of substructures against their parent halo density is lower than the density contrast of structures against the background, and this makes their identification more problematic. Even worse, the gravitational potential of a structure has a clear zero-point, given by the background density of the universe. So, it is well defined which particles are bound to the structure and what are unbound. Inside a structure, instead, such a definition is not clear: the background density of the structure varies inside them with the distance from the center, the dynamical state of the cluster, and the typical extend of the substructure itself. Therefore, telling that a particle is gravitationally bound to a given substructures involves a certain degree of arbitrariness, and an operational definition must be used.

A number of different *subhalo* finders now exist in the literature. Some are based on pure geometrical measures, other construct a candidate structure and apply an unbinding criteria, e.g. comparing the kinetic energy of a particle to its potential energy. A non-exhaustive list includes: hierarchical FOF (Klypin et al. 1999), Bound Density Maxima (Klypin et al. 1999), DENMAX (Bertschinger & Gelb 1991; Gelb & Bertschinger 1994), SKID (Weinberg et al. 1997; Stadel 2001), HOP (Eisenstein & Hut 1998), SUBFIND (Springel et al. 2001), MHF (Gill et al. 2004), ADAPTAHOP (Aubert et al. 2004), VOBOZ (Neyrinck et al. 2005), PSB (Kim & Park 2006), 6D FOF (Diemand et al. 2006), HSF (Maciejewski et al. 2009), AHF (Knollmann & Knebe 2009). Some of these algorithms are based on the FoF scheme, and vary the l parameter inside structures or apply the scheme to the full 6D phase space (hierarchical FOF, 6D FOF); some use the SO scheme, and apply an unbinding criterion (BDM, MHF, AHF); some use FoF to link particles to density maxima, and apply an unbinding (DENMAX, SKID); some introduce geometrical constraints, together with various unbinding procedure and phase space analysis (HOP, SUBFIND, ADAPTAHOP, VOBOS, PSB, HFS).

As far as the *DSC* detection is concerned, a further question

arises. The *DSC* is composed by stars *bound to the gravitational potential of the cluster and not to any galaxy*, and it is centrally concentrated. Many of its general properties, therefore, are primarily determined by the stars at the center of the cluster. It is therefore important to correctly distinguish *DSC* star particles from *cD* star particles. But such a distinction is often somewhat arbitrary, as in SKID, where the unbinding procedure is based upon the value of a parameter that must be given externally and whose effect must be tested *a-posteriori* (see M07). Other substructure finders, like SUBFIND, identifies all substructures but the main one and link all remaining star, gas and DM particles to the main subhalo, thus mixing *cD* and *DSC* stars. It is not even clear if a distinction between *cD* and its extended stellar halo is physically motivated or if it is all arbitrary.

In this work, we show that such two components can be distinguished in the velocity space. We use SUBFIND to identify substructures and disentangle galaxies from the *cD* + *DSC* stars. We show that the velocity distribution of the latter cannot be fit with a single Maxwellian distribution, while it is well fitted by a double Maxwellian (the sum of two Maxwellian distribution with different velocity dispersions).

We thus modify SUBFIND to perform an unbinding procedure on the *cD* + *DSC* stars. We use the gravitational potential given by the matter contained in a sphere, centered on the halo center, and we find a radius which divides the star particles in two populations whose velocity distribution is separately fit by a single Maxwellian. We vary the radius until the two resulting velocity dispersions correspond to the two velocity dispersion given by the double Maxwellian fit of the velocity distribution of the whole *cD* + *DSC* star population. We show that this procedure is able to disentangle the central galaxy from its extended stellar halo. We thus characterize the *DSC* through its phase-space distribution.

We then use our modified SUBFIND algorithm to repeat the M04 analysis of the *DSC* applied to a constrained cosmological simulation of the local universe. We also use two re-simulations of galaxy clusters, to test the behavior of our modified SUBFIND when we increase resolution. We compare results obtained using SUBFIND and SKID on this simulation, and show that they are in broad agreement, but dynamically separating the *cD* and the *DSC*, a Dependence of the *DSC* fraction on cluster mass is not found.

The plan of the paper is as follows. Section 2 describes our simulations. Section 3 shows the existence of two dynamically distinct stellar components, even at the center of galaxy clusters. Section 4 presents our scheme for disentangling such components. In Section 5 we apply our scheme to our local universe simulation, also comparing the results we obtain on the *DSC* properties with those obtained using SKID. In Section 6 we give our conclusions. In the Appendix we show a detailed comparison of the performance of SKID and SUBFIND for two galaxy clusters.

2 GENERAL SETUP

2.1 Simulations

The results presented in this paper have been obtained using the final output of a cosmological hydrodynamical simulation of the local universe. Our initial conditions are similar to those adopted by Mathis et al. (2002) in their study (based on a pure N-body simulation) of structure formation in the local universe. The galaxy distribution in the IRAS 1.2-Jy galaxy survey is first Gaussian smoothed on a scale of 7 Mpc and then linearly evolved back in

time up to $z = 50$ following the method proposed by Kolatt et al. (1996). The resulting field is then used as a Gaussian constraint (Hoffman & Ribak 1991) for an otherwise random realization of a flat Λ CDM model, for which we assume a present matter density parameter $\Omega_{0m} = 0.3$, a Hubble constant $H_0 = 70$ km/s/Mpc and a r.m.s. density fluctuation $\sigma_8 = 0.9$. The volume that is constrained by the observational data covers a sphere of radius ~ 80 Mpc/h, centered on the Milky Way. This region is sampled with more than 50 million high-resolution dark matter particles and is embedded in a periodic box of ~ 240 Mpc/h on a side. The region outside the constrained volume is filled with nearly 7 million low-resolution dark matter particles, allowing a good coverage of long-range gravitational tidal forces.

The statistical analysis made by Mathis et al. (2002) showed that, using this technique, the simulated $z = 0$ matter distribution provides a good match the large-scale structure observed in the local universe. Moreover, many of the most prominent nearby galaxy clusters like Virgo, Coma, Pisces-Perseus and Hydra-Centaurus, can be identified directly with halos in the simulation. Therefore the galaxy clusters in this simulations are an ideal target to study the diffuse stellar component, since observations are mainly bound to study objects in the local universe.

Unlike in the original simulation made by Mathis et al. (2002), where only the dark matter component is present, here we want to follow also the gas and stellar component. For this reason we extended the initial conditions by splitting the original high-resolution dark matter particles into gas and dark matter particles having masses of $0.48 \times 10^9 M_\odot/h$ and $3.1 \times 10^9 M_\odot/h$, respectively; this corresponds to a cosmological baryon fraction of 13 per cent. The total number of particles within the simulation is then slightly more than 108 million and the most massive clusters is resolved by almost one million particles. The gravitational force resolution (i.e. the comoving softening length) of the simulation has been fixed to be 7 kpc/h (Plummer-equivalent), fixed in physical units from $z=0$ to $z=5$ and then kept fixed in comoving units at higher redshift.

To get a handle on possible effects of resolution on our modified SUBFIND identification scheme for the *cD* and the *DSC*, we also analyzed two re-simulations of a massive galaxy clusters at higher resolution with exactly the same physics included. In the high resolution run (labeled as *3x* in the following) the individual particle masses are a factor of 3 times smaller than in our local universe simulation, and we scaled the softening accordingly to 5 kpc/h. Besides the most massive main halo ($M_{vir} \approx 2 \times 10^{15} M_\odot/h$), this re-simulation hosts several less massive halos ($M_{vir} \approx 1 \times 10^{14} M_\odot/h$), which we analyzed as well. In the extreme high resolution run (labeled as *18x* in the following) the individual particle masses are 18 times smaller and the softening is accordingly set to 2.5 kpc/h. Here, due to additional optimizations to the high resolution region of the re-simulation, only the main halo is suited to be analyzed. This cluster is resolved by more than respectively 4 and 25 million particles within the virial radius in the *3x* and the *18x* simulation.

Our simulations have been carried out with GADGET-2 (Springel 2005). The code uses an entropy-conserving formulation of SPH (Springel & Hernquist 2002), and allows a treatment of radiative cooling, heating by a UV background, and star formation and feedback processes. The latter is based on a sub-resolution model for the multiphase structure of the interstellar medium (Springel & Hernquist 2003). The code can also follow the pattern of metal production from the past history of cosmic star formation (Tornatore et al. 2004, 2007). This is done by computing the contributions from both Type-II and Type-Ia supernovae and energy

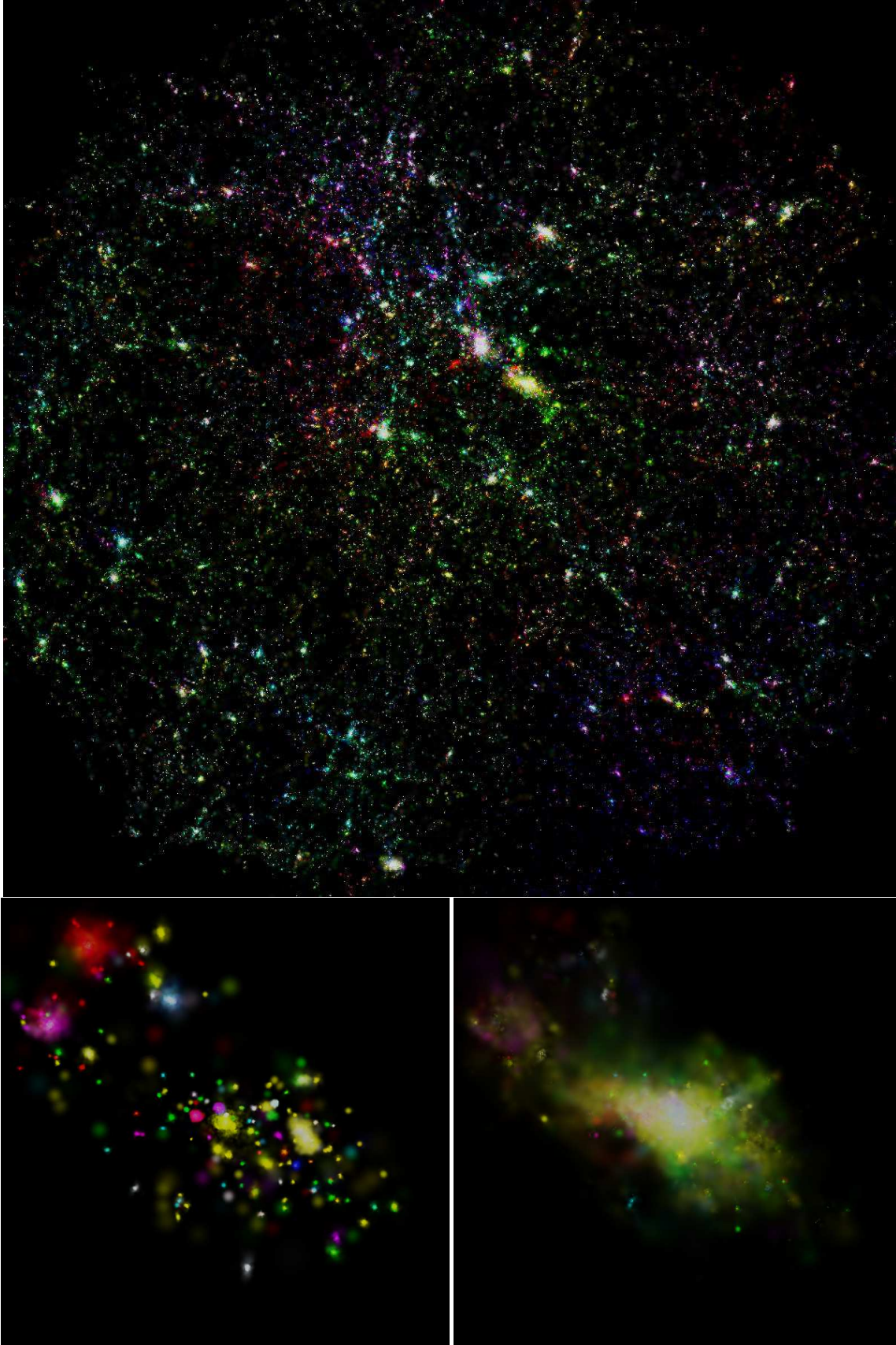


Figure 1. Visualization of the stellar component using the ray-tracing software SPLITCH. The color composition reflects the three-dimensional velocity field (see text for details), whereas the intensity reflects the stellar density. The upper panel shows all stars in the high-resolution sphere. The lower left panel shows all stars in galaxies (including the *cD*) of the most massive cluster, whereas the lower right panel shows all stars not bound to individual galaxies.

feedback and metals are released gradually in time, accordingly to the appropriate lifetimes of the different stellar populations. This treatment also includes, in a self-consistent way, the dependence of the gas cooling on the local metallicity. The feedback scheme assumes a Salpeter IMF (Salpeter 1955), and its parameters have been fixed to get a wind velocity of ≈ 480 km/s.

We note that our present local universe simulation has additional physics with respect to M04 work. Their mass resolution was $4.62 \times 10^9 h^{-1} M_\odot$ for a Dark Matter (DM) particle and $6.93 \times 10^8 h^{-1} M_\odot$ for a gas particles. The force resolution was $7.5 h^{-1}$ kpc (Plummer-equivalent softening length). While force and mass resolution are similar to those of our local universe simulation, M04 didn't include chemical enrichment and metal-dependent cooling.

2.2 Substructure detection

Substructures within halos are usually defined as locally over-dense, self-bound particle groups identified within a larger parent halo. In our analysis, the identification of these substructures is performed by applying a modified version of the SUBFIND algorithm (Dolag et al. 2009), which, in contrast to its original version (Springel et al. 2001) works with different particle species (e.g. dark matter, gas and star particles). Details on the algorithm can be found in (Springel et al. 2001; Dolag et al. 2009). In brief, as a first step, we employ a standard friends-of-friends (FoF) algorithm to identify the parent halos, with a linking length = 0.17 times the mean interparticle distance. Within each FoF group we then estimate the density of each particle species by adaptive kernel-interpolation, using the standard SPH approach with a given number of neighboring particles. Using an excursion set approach where a global density threshold is progressively lowered, we find locally over-dense regions within the resulting density field, which form a set of substructure candidates. The outer 'edge' of the substructure candidate is determined by a density contour that passes through a saddle point of the density field; here the substructure candidate joins onto the background structure. In a final step, all substructure candidates are subjected to a gravitational unbinding procedure where only the self-bound part is retained. We use all the particles initially belonging to the substructure candidate for evaluating the gravitational potential. For the gas particles we take also the internal thermal energy into account in the gravitational unbinding procedure. If the number of bound particles left is larger than a 20 particles, we register the substructure as genuine *sub-halo*. We define the stellar component of such *sub-halo* as a cluster member *galaxy*.

Although this works well for identification of satellite galaxies, all star particles not bound to any satellite galaxy are associated with the main halo stellar component, as the particles are always bound to the cluster potential. Therefore, this procedure does not split such a stellar population into the stars belonging to the central galaxy (*cD*) and to the stellar diffuse component (*DSC*).

Previous work (M04, M07) based on SKID (Stadel 2001) introduced an empirical distance scale to limit the part of the main halo used to calculate the potential and then distinguish between the *cD* and *DSC* by applying an unbinding criteria to this truncated potential. In section 3 we will show that the main halo stellar component has two components with two distinct dynamics. In section 4 we show that this can be used to modify the unbinding procedure to replace empirical distance scale by an inferred one, which optimize the splitting of the two components according to their dynamics.

To give an impression of the dynamics of the stellar com-

ponent in our simulations we modified the SPLOTCH package (Dolag et al. 2008), a Ray-tracing visualization tool for SPH simulations. Instead of mapping a scalar value to a color table, we mapped the three velocity components directly into the RGB colors. To obtain a logarithmic like scaling but preserve the sign of the individual velocity components we used a mapping based on the inverse of the hyperbolic sin function, e.g. $\langle r, g, b \rangle \propto \text{asinh}(v_{x,y,z})$. We calculated a smoothed density field based on all star particles using a SPH like kernel function. The resulting Ray-tracing images, are shown in Figure 1. The upper panel shows all stars in the high resolution sphere. Same color indicates the same 3 dimensional velocity direction, therefore the overall color pattern nicely reveals the large scale velocity structure within the cosmological simulation. The larger clusters however appear mostly white meaning that the internal velocity dispersion overcomes the ordered, large scale velocity pattern and therefore the color saturates into white. The lower left panel shows all stars in galaxies (including the *cD*) of the most massive cluster (the one with the yellowish halo also seen close to the center in the upper panel). This cluster has 238 satellite galaxies above our detection threshold. The different colors of the galaxies reflect their different orbital phase, whereas the yellow color of the *cD* and some other satellite galaxies reflects the large scale velocity field as seen in the upper panel. As expected, besides the mean velocity of the cluster, there is no large scale pattern visible in the galaxy orbits. Also the individual galaxies show a clear color indicating that the individual velocity dispersion of the stars within the galaxies is much smaller than their orbital motion within the galaxy cluster. The lower right panel shows all stars not bound to individual galaxies. The small scale structures remaining in the *DSC* are either galaxies below our detection threshold, or the outer envelopes of large cluster members, which are not bound to the galaxies. Notice the pink, ring like structure to the upper left, which can be associated to the group of infalling galaxies visible at the same position with the same color in the left panel. However, most of the *DSC* appears homogeneously in white and yellow colors, indicating a mean velocity similar to the *cD* and to the large scale velocity field, but a larger velocity dispersion.

3 DISTINGUISHING DIFFERENT DYNAMICAL STELLAR COMPONENTS

3.1 The different stellar components

As shown in M07, the *DSC* within $0.5 R_{\text{vir}}$ forms mainly by merging of satellite galaxies with the *cD* galaxy. Therefore one could expect that the *DSC* still reflects the dynamics of the satellite galaxies and thus might have a velocity dispersion close to that of the satellite galaxies. On the other hand, the stars belonging to the *cD* galaxy will have a much smaller velocity dispersion due to the relaxation and merging processes, which should get rid of the excess orbital energy in order to form the galaxy. Indeed, the main halo stellar component shows clear signs of a bimodal distribution. Figure 2 shows the histogram of the modulus of velocities ("velocities" hereafter) of the stellar component of the main halo for one of the more massive cluster of the simulation. This distribution reveals its bi-modality as it can be well fitted by the superposition of two Maxwellian distributions

$$N(v) = k_1 v_1^2 \exp\left(-\frac{v_1^2}{\sigma_1^2}\right) + k_2 v_2^2 \exp\left(-\frac{v_2^2}{\sigma_2^2}\right), \quad (1)$$

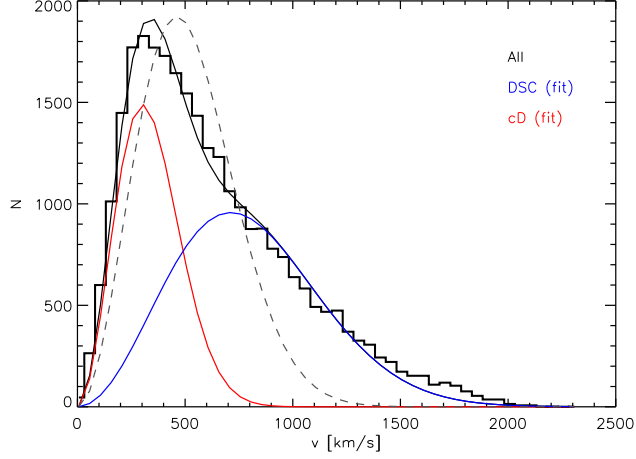


Figure 2. Velocity histogram (black histogram) of the main halo stellar component and a double Maxwellian fit to it (black line). The red and the blue line are showing the individual Maxwellian distributions of the two components. The gray, dashed line is our best fit with a single Maxwellian.

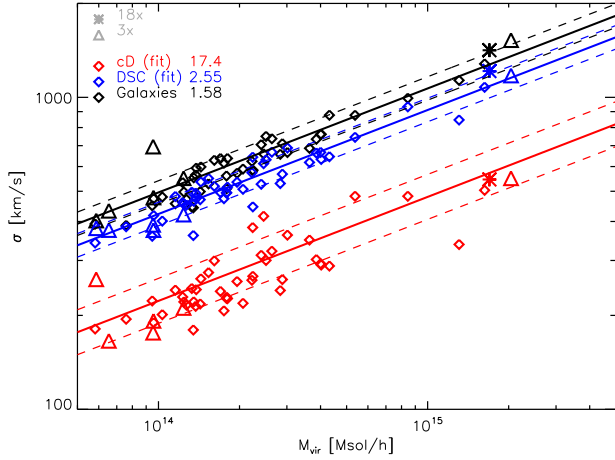


Figure 3. Velocity dispersion of the three stellar components (*DSC*, *cD* and galaxies) as a function of the virial mass of the galaxy cluster for the sample of 44 clusters with at least 20 satellite galaxies. The velocity dispersion of the *DSC* (blue symbols) is only slightly smaller than the one of the galaxies (black symbols), whereas the velocity dispersion of the *cD* stars (red symbols) is significantly smaller. The dashed lines show the one sigma scatter of our best fit relations. Velocity dispersion shows here are obtained using the double Maxwellian fit 1.

For comparison, we also show in Figure 2 the single Maxwellian distribution which best fits our data. It is clear that while a single Maxwellian is a poor fit to the velocity distribution of the stellar component of our main halo, a double Maxwellian is a very good one.

In itself, this does not allow to identify which star particle belongs to the *cD* and which to the *DSC* but it already allows to draw conclusions based on the statistical properties of the two distributions. Therefore we selected from our simulation all clusters having at least 20 identified satellite galaxies, ending up with a sample of 44 galaxy clusters. For each of them we fitted a double Maxwellian to the velocity distribution of the main halo stellar component. Note that in all cases the fits are quite good, and introducing a third

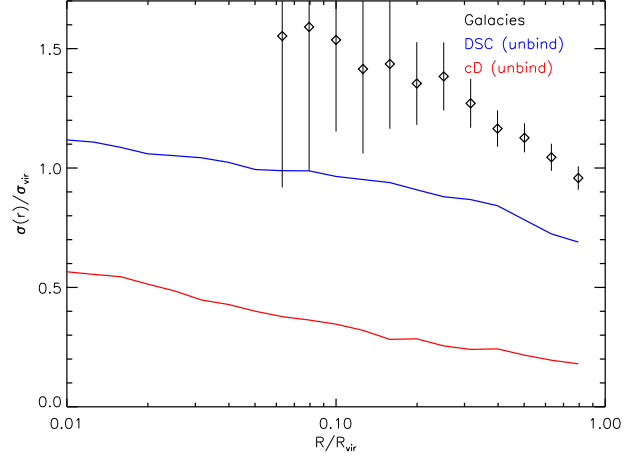


Figure 4. Shown are the results from stacking all 44 clusters of our sample. Plotted is the radial velocity dispersion (in virial units) for the *DSC* and the *cD* component, as well as for the satellite galaxies. The error bars at the symbols for the galaxies are statistical errors based on the number of galaxies within each radial bin.

Maxwellian component does not improve them, as the amount of star particle associated to such third component always stays at the percent level, and just reflects structures like the outer envelope of large, in-falling groups.

We hypothesize that the two Maxwellian distribution of our fits correspond to two distinct stellar components, namely the *cD*, associated with the smaller velocity dispersion, and the *DSC* having a larger one. Figure 3 shows the velocity dispersion of such two stellar components, together with the velocity dispersion of the galaxy population of each cluster, as a function of the virial mass of the galaxy cluster for our sample. The velocity dispersion of the *DSC* is only slightly smaller than the one of the galaxies: another hint on the origin of the *DSC* component from merging satellite galaxies. The slightly smaller velocity dispersion could indicate that either some momentum transfer occurred during the merger event with the *cD*, or the galaxies which contributed to the build up of the *DSC* till redshift zero have a slightly lower velocity dispersion than the average galaxy population. The latter could be the case, since such galaxies might be mostly on radial orbits which lead to an earlier destruction by interactions with the *cD* than the (still) remaining galaxies within the cluster. However, since the *DSC* is more centrally concentrated than galaxies, they could sample different region of clusters and thus have slightly different dynamics. Figure 4 shows the radial velocity dispersion profile stacking all 44 clusters of our sample. From this analysis it appears that the dynamical differences are evidently the same at all radii, again indicating that they not just sample different regions inside the cluster but have different dynamical origins.

If the creation of the *DSC* would be a continuous process, one would expect a small scatter in the relation between virial mass of the cluster and velocity dispersions for the *DSC* component, specially compared to that for galaxies, as they are much less numerous. However, from Figure 3, this does not seem to be the case, where we find a scatter of $\approx 9\%$ for the galaxies, $\approx 9\%$ for *DSC* and $\approx 18\%$ for the *cD*, again indicating that the production of the *DSC* originates in individual, violent events such as mergers with the *cD*. The velocity dispersion of the *cD* component is significantly lower,

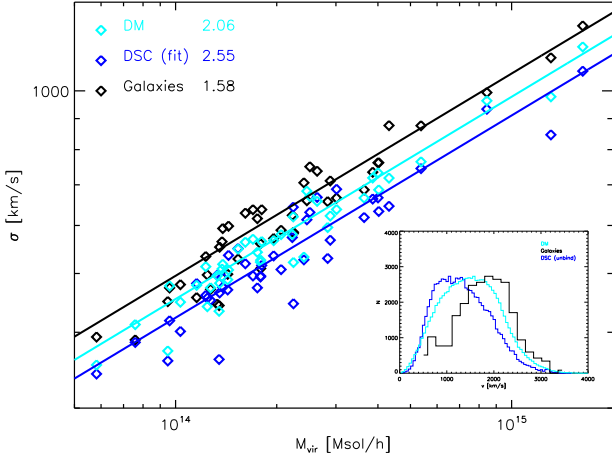


Figure 5. Same as Figure 3, but comparing the velocity dispersions of *DSC* component, galaxies and dark matter. We also report the value of the normalization A for the best fit to equation 2. The inlay shows the individual velocity histograms for the three components obtained from the most massive cluster.

and shows an even larger scatter. In Figure 3, solid lines represent the best fit to

$$M = A \left(\frac{\sqrt{3}\sigma}{10^3 \text{ km/s}} \right)^3 \times 10^{14} M_\odot/h \quad (2)$$

with a normalization A of 1.58, 2.55 and 17.4 for galaxies, *DSC* stars and *cD* stars respectively. The value of A we obtain for galaxies is in line with the results presented in Biviano et al. (2006).

3.2 The different dynamical tracers

Although the differences in the velocity dispersion between the galaxies and the *DSC* component as seen in Figure 3 are small – basically of the size of the RMS scatter of the correlation – they seem to be systematic. Therefore, the question rises of which of the two distribution traces the underlying dark matter best. Figure 5 shows the velocity dispersion of dark matter, galaxies and the *DSC* component for the full set of analyzed galaxy clusters. Interestingly, the velocity dispersion of the dark matter falls between the one of the *DSC* component and the one of the galaxies. The best fit to equation 2 gives a normalization A of 1.58, 2.06 and 2.55 for galaxies, dark matter and *DSC* respectively. The inlay shows the velocity histogram (arbitrarily normalized) of the *DSC*, the galaxies and the dark matter within the most massive cluster in the simulation, clearly revealing the systematic differences among the three different components. Note that we had to apply our identification scheme, described in section 4, to obtain the velocity distribution of the individual stars associated with the *DSC*.

3.3 The Mass in the different stellar distributions

Having the velocity distribution given by our double Maxwellian fit, we can also evaluate the total stellar mass associated to the two individual populations by just integrating separately over the two distribution functions which sums up in the double Maxwellian fit. Figure 6 shows the stellar mass associated to the *DSC* compared to the *cD* component. From this estimate follows that the simulations predict the mass within the *DSC* to be, on average, slightly

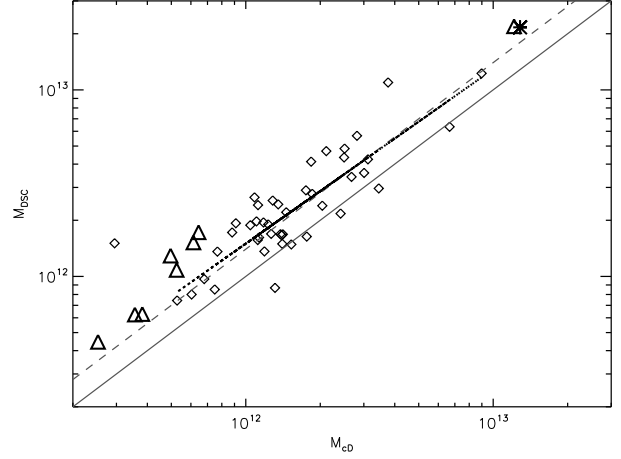


Figure 6. Relation between the *DSC* stellar mass and *cD* mass. The solid line marks a one to one relation. On average, the *DSC* has ca. 15% more mass than the *cD*, as indicated by the dashed line. The dotted line represent the best fit linear relation excluding the one identification with extreme low *cD* mass as it would over proportional alter the fit.

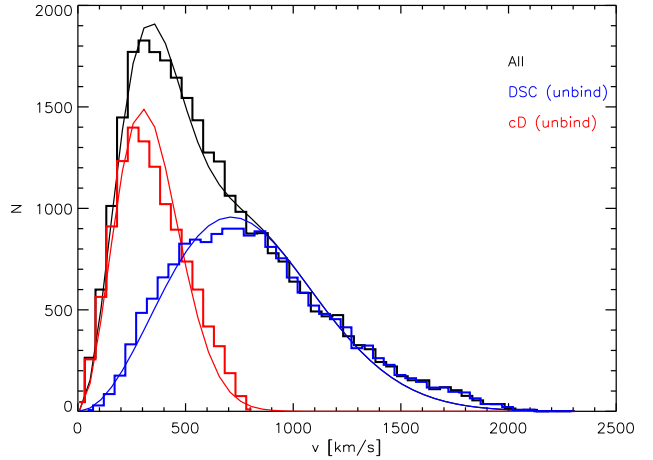


Figure 7. As in figure 2, velocity histogram (black line) of the main halo stellar component and a double Maxwellian fit to it (gray line) is shown. Red and blue histograms show the velocity distribution of the *cD* and *DSC* stars after the un-binding procedure, together with the two individual Maxwellian distributions from the global fit, respectively.

larger than the mass in the *cD* galaxy, by $\approx 15\%$, as indicated by the dashed line in figure 6. From this result follows that the mass fraction of the two dynamically identified components associated with the *DSC* and the *cD* will not depend on the mass of the galaxy cluster, being their ratio constant.

This is different from previous findings (e.g. M04, Sommer-Larsen et al. (2005)), and it is a feature of the dynamically based separation of these two components, as we will discuss in detail later.

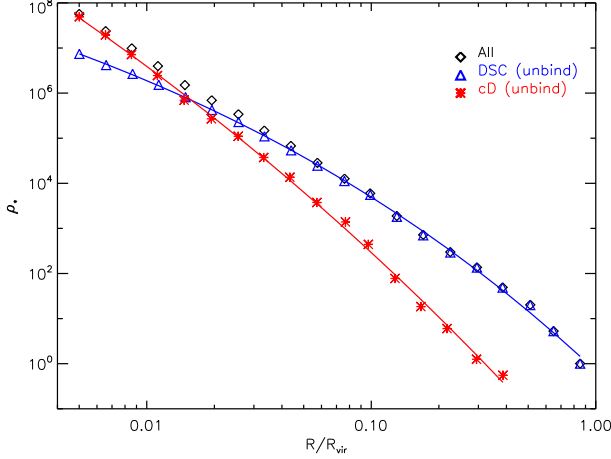


Figure 8. Main halo (black symbols), *cD* (red symbols) and *DSC* (blue symbols) stellar density profiles. The red and blue line are a Sersic fit to the two distributions, respectively.

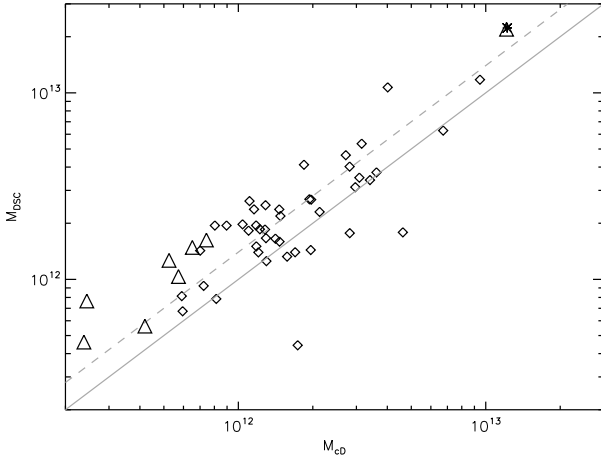


Figure 9. Relation between *DSC* and *cD* stellar mass, after the unbinding. The mean relation is the same, but the scatter increases significantly.

4 SPLITTING CD AND DSC COMPONENTS

After detecting two distinct components, which we identify as *cD* and *DSC*, in the velocity distribution of the stellar population, we need a way to assign the individual star particles to one of them.

To perform this task, we start from a given fiducial radius (initially assumed to be a fraction of the virial radius) and, as a first step, we calculate the gravitational potential given by all particles within this fiducial radius and apply the un-binding to the particles of the main halo component. As a second step, we separately fit the velocity distribution of each of the two stellar populations, classified as “bound” and “unbound” in the first step, to a Maxwellian distribution, obtaining two velocity dispersions σ_b^2 , σ_{ub}^2 .

We compare σ_b^2 and σ_{ub}^2 to the dispersions obtained from the original, double Maxwellian fit performed on the total star component of the main halo, σ_1^2 and σ_2^2 . We then increase or decrease the radius for the unbinding procedure, trying to match σ_1^2 and σ_2^2 . Using this new radius and re-computing the gravitational potential, the procedure is repeated until the velocity distributions of the two

Component	σ	I_0	A	α
<i>cD</i>	226	23.3	26.0	10.5
<i>DSC</i>	516	11.5	11.7	5.7

Table 1. Table giving the parameters for the Sersic fit of the two components and the velocity dispersion from the double Maxwellian fit.

components converges onto the two velocity distributions inferred from the original, global fit: $\sigma_{ub} \cong \sigma_1$ and $\sigma_b \cong \sigma_2$. We usually adjust the radius to match the value σ_1 of the *DSC* component, but if the algorithm does not converge, we try a second time using the dispersion σ_2 of the *cD* component. The iterative procedure stops when σ_{ub}/σ_1 (or σ_b/σ_2) differs from one less than a given threshold value. Note that our iterative procedure tries to match *one* velocity dispersion at a time; the fact that, doing so, we also obtain the correct value of the other velocity dispersion is not given a-priori. Usually both dispersions agree within percent level within less than ten iterations.

Figure 7 shows, similarly to figure 2, the velocity histogram of the main halo stellar component (black line) in the same, massive cluster of the simulation, fitted by the superposition of two Maxwellian distributions (solid lines). We also show the histograms of the bound stellar particles belonging to the *cD* component (red histogram) as well as the unbound stellar component associated to the *DSC* (blue histogram). Clearly, the two components are well identified and separated by this procedure.

Once we identify the individual stars in the two distributions, we can plot their radial density profile. Figure 8 shows the radial density profiles of the *cD* and *DSC* component respectively, as well as a fitted Sersic profile

$$\log(\rho_*) = I_0 - A \left(\frac{r}{R_{vir}} \right)^{(1/\alpha)}. \quad (3)$$

We find that both profiles are fitted quite well by individual Sersic profiles and therefore the total, radial stellar density profile can be described as a superposition of two Sersic profiles. Also, in line with previous finding of M04, the profile of the *cD* component is much steeper and less curved than that of the *DSC* component. Therefore, also using our new SUBFIND identification scheme for the *DSC*, we find excess light at large radii with respect to the *cD* Sersic profile. For the best fit parameters, see table 1.

Comparing the velocity dispersions σ_1, σ_2 inferred from the original, double Maxwellian fit to all the main halo stars and the two dispersions σ_b, σ_{ub} for *cD* as well as the *DSC* we find a very tight relation. In almost all cases the iteration was successfully based on the *DSC* component, which led to a scatter below our chosen threshold. Although the dispersions of the inferred *cD* component match very well the corresponding ones of the double Maxwellian fit, the scatter is slightly larger. It is difficult to say if an improvement of the iteration procedure could further reduce this scatter or if it is intrinsically due to our un-binding scheme. In effect, the very fact that unbinding star particles using the matter contained in a sphere of a given radius divides them into two sets, whose velocity distributions match the two component of the overall double Maxwellian distribution is not a-priori guaranteed. We regard to this match as a hint that the double Maxwellian shape of the overall star particle distribution is really produced by the interplay of two well separated gravitational potentials, the cluster one and the central galaxy one.

Figure 9 shows the relation between the stellar mass within the *DSC* and the *cD* component, like Figure 6. This time we directly

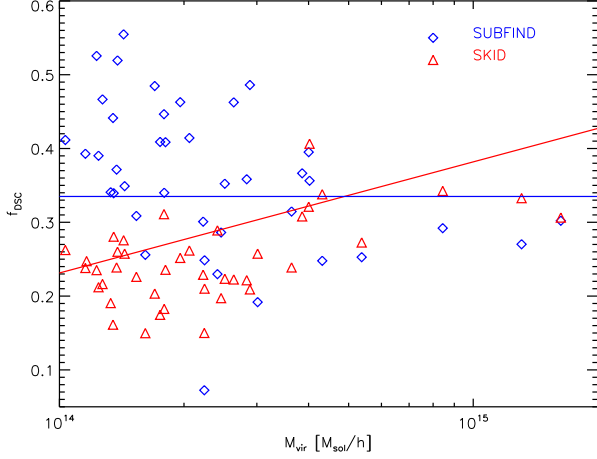


Figure 10. Fraction of stellar mass in *DSC* as a function of the galaxy cluster virial mass. Blue diamonds show the *DSC* fractions as given by our new SUBFIND+un-binding algorithm, red triangles show the *DSC* fractions as obtained using SKID. The red line shows the result of a least-chi-squared fit of the SKID fractions to the linear function $F_{DSC} = b \cdot M_{clus} + a$, which gives $a = 0.211$, $b = 1.0310^{-16}$, $\sigma_a = 0.01$, $\sigma_b = 2.5910^{-17}$, $\chi^2 = 0.112$. Performing the same fit using the SUBFIND fractions gives a value of b compatible with zero at 1.5σ , we thus fit SUBFIND *DSC* fractions to a constant function $b = 0.335 \pm 0.02$ (blue line)

use the mass of our two components, as obtained by our unbinding scheme. As before, the dashed line indicates an 15% higher mass in the *DSC* than in the *cD* component.

A larger scatter in the masses of the *cD* obtained from the unbinding compared to the ones calculated from the velocity distributions is clearly visible. Beside this, there is no bias associated with our unbinding scheme: it seems able to disentangle two component whose properties are identical to those inferred from the velocity distribution of the whole stellar population.

In Figure 6,7 and 9 we also report results obtained from two individual galaxy cluster re-simulations (using different symbols, as indicated in the plots), which have 3 and 18 times better mass resolution. Such results are perfectly in line with those obtained from the cosmological simulations. Thus, our unbinding scheme appears to be stable against resolution effects. Note that, at variance with other schemes, e.g SKID, we don't have any parameter to be tuned when resolution is changed. However, we excluded these points from the fits presented in Figure 8.

5 PROPERTIES OF THE *DSC* IN THE SIMULATED LOCAL UNIVERSE

We now apply our new un-binding scheme to all 44 massive clusters in the local universe simulation with at least 20 member galaxies. In all cases, Sérsic profiles are a good fit to the radial density profiles of *cD* and *DSC* populations separately, as already shown for one massive cluster in Figure 8. Also, as expected, the *cD* component in all systems is radially more concentrated than the *DSC*. From inspecting the radial density profiles of the separated components we find that the *DSC* component in all cases dominates at radii larger than $0.03\text{--}0.08 R_{vir}$ and contributes less than 10% to the stellar density in the center.

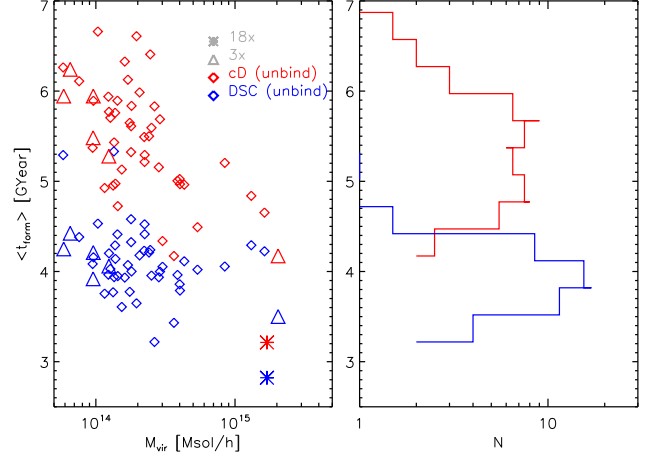


Figure 11. The left panel shows the mean formation times of *cD* (red symbols) and *DSC* (blue symbols) as function of the virial mass of the cluster. The right panel shows the histograms of the distribution of the mean formation times for the *cD* and the *DSC* components, respectively.

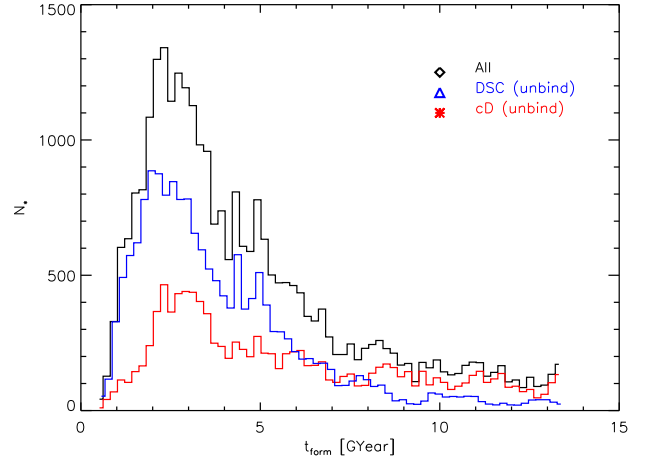


Figure 12. Formation time of main sub-halo stars (black histogram), *cD* stars (red histogram) and *DSC* stars (blue histogram) in the most massive cluster in the cosmological simulation.

5.1 Comparison with previous works

Figure 10 shows the fraction of stellar mass in the *DSC* against the cluster virial mass. To make a significant comparison with M04 results, we also analyzed the local universe simulation using SKID, repeating the same procedure described there (see also Appendix for details). We remind the reader that M04 analyzed a cosmological box of size $192h^{-1}$ Mpc, run with mass and force resolution similar to those used here, but different physics: in particular, they didn't follow chemical enrichment and didn't use a metal-dependent cooling function.

Nevertheless, we recover the trend of having a larger *DSC* fraction in larger clusters when we define it using SKID, even if such a trend is weaker here than in M04. Our new dynamical identification of the *DSC*, however, gives a different results. Although the *DSC* fractions for the most massive cluster agree well, on average they are higher than those found using SKID, especially at

low cluster masses, and, moreover, we can't detect any trend with the cluster mass. In Appendix, we show a detailed comparison of one high mass and one low mass cluster analyzed with both methods to demonstrate that this effect is indeed related to the fact, that for the SKID analysis a scale has to be given a-priori, which could lead to this effect. However, we want to stress once more that the *DSC* mass fraction found here should not be regarded as immediately comparable to observations. Especially in low-mass clusters, the *DSC* abundance is expected to be dominated by central regions. Central regions are exactly those where a dynamical identification of a *DSC*, as that presented here, can most differ from a surface brightness based detection of an *ICL* components. Dynamical analysis of the *DSC* should instead be regarded as attempts to determine its physical properties and its origin.

5.2 Different stellar populations in *cD* and *DSC*

In line with M04, we find that the stellar populations of the two different components, however we identify them, differ significantly not only in their spatial distribution, but also in their history.

The left panel of Figure 11 shows mean formation times of the stars in the *cD* (red symbols) and *DSC* (blue symbols) for our sample of 44 clusters as obtained using our new procedure. In the *DSC* (and therefore its progenitor galaxies), there is no significant star formation within the last 4-5 Gyrs, while the *cD* population is on average younger. The difference in the two age distributions is also clear from the right panel of Figure 11, where we show the histograms of mean formation times for the *cD* (red) and *DSC* (blue). This agrees with the finding of M07, that *DSC* is mainly formed during merger processes which also form the central galaxy of each cluster. Destroyed satellite galaxies, and pre-processed stars, already unbound in merging galaxy groups, goes to the *DSC* of clusters, whereas the *cD* still can form stars at low rate at recent times. In numerical simulation of galaxy clusters, one known issue is the excess star formation at the center of cooling flows, producing an overly blue central galaxy, see e.g. Saro et al. (2006). Real BCGs have a much lower low- z star formation rate, therefore we expect this age segregation to be smaller in reality; by how much, is still to be completely understood. Note, however, that this mechanism applies to *all* mergers at *all* times. Therefore, also at higher redshifts, the merger remnants at the center of proto-clusters will have ongoing star formation while, obviously, the mean age of the produced *DSC* will grow older. This can be seen from Figure 12 where we show, for the most massive cluster in the cosmological simulation, the distribution of formation times of star particles for all stars in the main sub-halo, *cD* stars and *DSC* stars. Star particles older than 7 Gyr (i.e., $t_{\text{form}} < 6$) are abundant in the *DSC*; these stars formed at redshifts $z > 1$ and must have become unbound before. At late-times, lack of feedback in the simulations lead to ongoing star formation at the center of the cluster gives an excess of young stars ($t_{\text{form}} > 8$ Gyr) in the *cD*. However, even ignoring all stars with $t_{\text{form}} > 8$ Gyr, the difference between the average formation time of *cD* and *DSC* still remains half of the effect shown in figure 11.

As before, we added in figure 11 the results obtained using our two re-simulations of individual galaxy clusters. Again, they reproduce the trends found in our cosmological simulations, and for the same reasons as before, we did not include them in the histograms. Note that, especially in the very high resolution run, star formation is slightly shifted to earlier times, as expected since such a simulation resolves the first star-forming structures better.

We also evaluated mean formation times of *cD* and *DSC* stellar

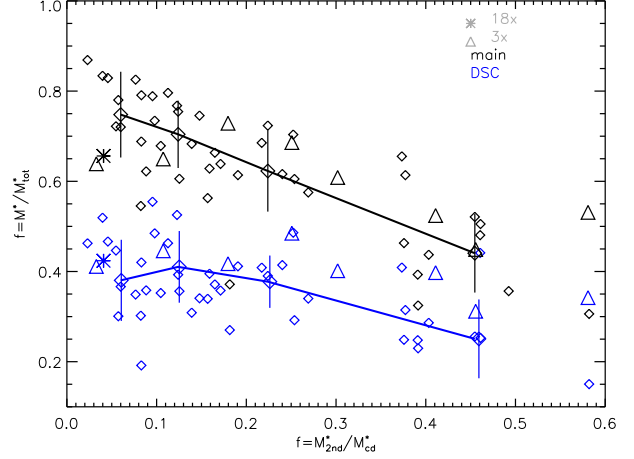


Figure 13. Fraction of stellar in the main sub-halo, the *DSC* and the *cD* component, respectively, to the total mass in stars as a function of the fraction of the stellar mass of the second brightest galaxy in each cluster to the *cD* mass.

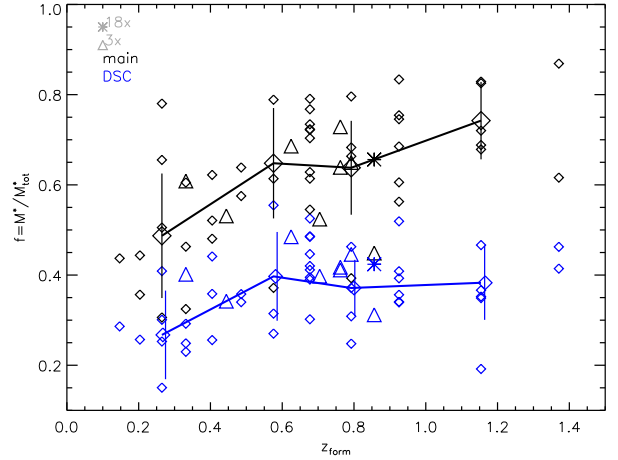


Figure 14. Same as figure 13 but as a function of the formation redshift, defined as the redshift at which the mass of the main progenitor is half of the mass of the descendant cluster at redshift zero.

populations given by SKID for our 44 clusters. The result is similar to that shown for SUBFIND in Figure 12, but mean formation times of the two components are closer with the average formation time of *cDs* being 4.9 Gyr and that of *DSC*, 4.1 Gyr. Again, this suggests that SKID is less efficient in disentangling the two components, and assign to some *cD* star particles which have properties typical of the *DSC*.

5.3 Origin of the scatter of the *DSC*

Both observations and previous numerical works indicated that the fraction of the *DSC* component in clusters having similar mass shows a large scatter. Reminding the reader that our cluster set is a complete, e.g. volume limited sample, we can try to investigate where the scatter in relations of *cD* and *DSC* components with the cluster mass comes from. Thus, we calculated the the total mass for our different stellar components, namely the total amount of

formed stars, the amount of stars in the main sub-halo and the stellar mass of *DSC* and *cD* components respectively. In line with previous findings (Borgani et al. 2006), there is a weak trend to form more stars in smaller clusters, but the scatter of formed stars in similar mass systems is quite small. Although the global trends is reflected more or less homogeneously in all different components, the relative scatter, especially in the main and *DSC* component is quite substantial.

As seen before, the un-binding procedure induce additional scatter by itself; however this does not account for the whole variation of the *DSC* fraction among different systems of similar mass. Figure 13 shows the fraction of all stars in the main sub-halos and in the *DSC*, as a function of the relative importance of the second most massive galaxies within each cluster. There is a clear indication that the presence of a quite massive second galaxy (indicating a young system, where the remain of the last major merger has not yet merged with the *cD*) is related to a less prominent *DSC* component. Note that this is fully compatible with the low fraction of *ICL* observed in the Virgo cluster ($< 10\%$), where the observed importance of the two brightest galaxies is quasi equal. Therefore the observed Virgo cluster lies even to the right of the shown range in figure 13.

By constructing the merger tree of our set of clusters we can trace back the main progenitor of each of the cluster. Adopting the common definition for the redshift of formation of a cluster z_{form} (redshift at which the main progenitor of the cluster has half of its final mass) we can check how the stellar fractions in the different components depend on the age of the cluster. Figure 14 shows the stellar fraction of the main sub-halos and the *DSC* component as a function of the formation redshift z_{form} . In old systems, expected to be very relaxed, the growth of the *cD* galaxy seems to be the dominant source of increasing the stellar fraction, whereas the *DSC* seems not be evolving significantly. Only in very young systems the *DSC* shows a deficit, most likely because the merging is still ongoing and the *DSC* is not yet released from the progenitors of the forming systems.

Summarizing, when we apply our new un-binding scheme, a correlation of the *DSC* with the cluster mass is not present at all. The amount of diffuse stars appears to depend more on the formation redshift of the cluster and on its dynamical state: more relaxed and evolved clusters have more *DSC* because they had more time to complete the merging of galaxies onto the *cD*.

6 CONCLUSIONS

We showed that the stellar populations of the main sub-halos of massive galaxy clusters in cosmological, hydrodynamical simulations are composed of two, dynamically clearly distinct components. Their velocity distributions can be fitted by a double Maxwellian distribution. Including this information into an un-binding procedure, we were able to spatially separate the two components in a central galaxy (*cD*) and a diffuse stellar component (*DSC*). The latter can be associated with the observationally very interesting intra cluster light (*ICL*) component. However, we want to stress that there are significant differences in how the *ICL* is measured in observations and how the *DSC* is inferred in simulations. Therefore a detailed comparison of the amount of this stellar component of galaxy clusters in simulations and observations can only be done by mimicking observational strategies, e.g. inferring the component from synthetic surface brightness maps.

On the other hand our un-binding algorithm is ideally suited

to study the physical processes leading to liberate the *DSC* as it allows to distinguish the *DSC* and the *cD* with a minimum set of assumptions, namely

- The stars of the *cD* component are those gravitationally bound to the inner most part of the halo, i.e. to the galaxy itself.
- The stars of the *cD* and the *DSC* reflect two dynamical distinct populations.

These two assumptions naturally reflect our expectations that the *cD* galaxy is a relaxed object sitting in the center of the cluster potential, while *DSC* is mainly formed by violent mergers of satellite galaxies with the *cD*, is in equilibrium with the overall gravitational potential of the cluster, and still holds memory of the dynamics of the satellite galaxies.

We show that our un-binding scheme is able to disentangle two stellar populations, *cD* and *DSC*, whose velocity distributions separately matches the two components of the double Maxwellian velocity distribution which characterizes the stars belonging to the main sub-halos of clusters.

Applying our algorithm to a cosmological, hydrodynamical simulation of the local universe including cooling and star formation, we found that

- The velocity dispersion associated to the *DSC* component is comparable to the velocity dispersion of the member galaxies, whereas the velocity dispersion associated to the *cD* is significant smaller (by a factor of ≈ 3). This implies that the *DSC* dynamics is determined by the general gravitational potential of the cluster, while the *BCG* one feels the local galactic potential.
- In line with previous findings, the spatial distribution of the star particles belonging to the *cD* are much more concentrated than the one of the *DSC*, which starts to dominate the stellar density at radii larger than $0.03\text{--}0.08 R_{\text{vir}}$.
- The formation time of the star particles associated with the *cD* is significant smaller than the one of the *DSC*, indicating that – in line with previous findings – the *DSC* is older (on average $\approx 1.5\text{Gyears}$).
- The fraction of the stars within the *DSC* is only weakly dependent on the mass of the galaxy cluster, however, we find a larger fraction in clusters with a early formation time. This is in line with previous findings that the *DSC* originates from the late stages of merger events of galaxies with the *cD*. Therefore clusters which have had enough time to liberate stars since the last major infall show a larger *DSC*. Interestingly, the mass ratio between the second brightest cluster galaxy and the *cD* galaxy can be used as a proxy for the time till the last major merger. Using such a ratio, we obtain an even stronger trend: clusters with a small ratio show a large *DSC* fraction, whereas clusters with a large ratio did not have yet enough time to liberate the stars contribution to the *DSC*. We expect that such a trend could also be detected in *ICL* observations.

We conclude that the separation of the *cD* and the *DSC* in simulations, based on our dynamical criteria, is more opportune than other current methods, as it depends on less numerous and physically more motivated assumptions, and leads to a stable algorithm helping to understand the different stellar components within galaxy clusters.

ACKNOWLEDGMENTS

The hydrodynamical simulations on which the presented work is based on have been performed using computer facilities at the Uni-

versity of Tokyo supported by the Special Coordination Fund for Promoting Science and Technology, Ministry of Education, Culture, Sport, Science and Technology. K. D. acknowledges the supported by the DFG Priority Programme 117, the hospitality of the Department of Astronomy of the University of Trieste, the receipt of a “Short Visit Grant” from the European Science Foundation (ESF) for the activity entitled “Computational Astrophysics and Cosmology” and the financial support by the “HPC-Europa Transnational Access program”. This work has been partially supported by the PRIN-MIUR grant “The Cosmic Cycle of Baryons”, by the INFN-PD51 grant and by a ASI-COFIS theory grant.

REFERENCES

- Arnaboldi M., Freeman K. C., Mendez R. H., Capaccioli M., Ciardullo R., Ford H., Gerhard O., Hui X., Jacoby G. H., Kudritzki R. P., Quinn P. J., 1996, *ApJ*, 472, 145
- Arnaboldi M., Freeman K. C., Okamura S., Yasuda N., Gerhard O., Napolitano N. R., Pannella M. E., 2003, *AJ*, 125, 514
- Arnaboldi M., Gerhard O., Aguerri J. A. L., Freeman K. C., Napolitano N. R., Okamura S., Yasuda N., 2004, *ApJ*, 614, L33
- Aubert D., Pichon C., Colombi S., 2004, *MNRAS*, 352, 376
- Bertschinger E., Gelb J. M., 1991, *Computers in Physics*, 5, 164
- Biviano A., Murante G., Borgani S., Diaferio A., Dolag K., Girardi M., 2006, *A&A*, 456, 23
- Borgani S., Dolag K., Murante G., Cheng L.-M., Springel V., Diaferio A., Moscardini L., Tormen G., Tornatore L., Tozzi P., 2006, *MNRAS*, 367, 1641
- Byrd G., Valtonen M., 1990, *ApJ*, 350, 89
- Castro-Rodríguez N., Aguerri J. A. L., Arnaboldi M., Gerhard O., Freeman K. C., Napolitano N. R., Capaccioli M., 2003, *A&A*, 405, 803
- Castro-Rodríguez N., Arnaboldi M., Aguerri J. A. L., Gerhard O., Okamura S., Yasuda N., Freeman K. C., 2009, *ArXiv e-prints*
- Davis M., Efstathiou G., Frenk C. S., White S. D. M., 1985, *ApJ*, 292, 371
- Diemand J., Kuhlen M., Madau P., 2006, *ApJ*, 649, 1
- Doherty M., Arnaboldi M., Das P., Gerhard O., Aguerri J. A. L., Ciardullo R., Feldmeier J. J., Freeman K. C., Jacoby G. H., Murante G., 2009, *A&A*, 502, 771
- Dolag K., Borgani S., Murante G., Springel V., 2009, *MNRAS*, pp 1314+
- Dolag K., Reinecke M., Gheller C., Imboden S., 2008, *NJOP*, submitted
- Durrell P. R., Ciardullo R., Feldmeier J. J., Jacoby G. H., Sigurdsson S., 2002, *ApJ*, 570, 119
- Eisenstein D. J., Hut P., 1998, *HOP: A New Group-Finding Algorithm for N-Body Simulations*
- Feldmeier J. J., Ciardullo R., Jacoby G. H., Durrell P. R., 2004, *ApJ*, 615, 196
- Feldmeier J. J., Mihos J. C., Morrison H. L., Harding P., Kaib N., Dubinski J., 2004, *ApJ*, 609, 617
- Feldmeier J. J., Mihos J. C., Morrison H. L., Rodney S. A., Harding P., 2002, *ApJ*, 575, 779
- Frenk C. S., White S. D. M., Davis M., Efstathiou G., 1988, *The formation of dark halos in a universe dominated by cold dark matter*
- Gal-Yam A., Maoz D., Guhathakurta P., Filippenko A. V., 2003, *AJ*, 125, 1087
- Gelb J. M., Bertschinger E., 1994, *ApJ*, 436
- Gerhard O., Arnaboldi M., Freeman K. C., Kashikawa N., Okamura S., Yasuda N., 2005, *ApJ*, 621, L93
- Gerhard O., Arnaboldi M., Freeman K. C., Okamura S., Kashikawa N., Yasuda N., 2007, *A&A*, 468, 815
- Gill S. P. D., Knebe A., Gibson B. K., 2004, *MNRAS*, 351, 399
- Gnedin O. Y., 2003, *ApJ*, 589, 752
- Gonzalez A. H., Zabludoff A. I., Zaritsky D., Dalcanton J. J., 2000, *ApJ*, 536, 561
- Gonzalez A. H., Zaritsky D., Zabludoff A. I., 2007, *ApJ*, 666, 147
- Hoffman Y., Ribak E., 1991, *ApJ*, 380, L5
- Kim J., Park C., 2006, *ApJ*, 639, 600
- Klypin A., Gottlöber S., Kravtsov A. V., Khokhlov A. M., 1999, *ApJ*, 516, 530
- Knollmann S. R., Knebe A., 2009, *ApJS*, 182, 608
- Kolatt T., Dekel A., Ganon G., Willick J. A., 1996, *ApJ*, 458, 419
- Krick J. E., Bernstein R. A., 2007, *AJ*, 134, 466
- Krick J. E., Bernstein R. A., Pimbblet K. A., 2006, *AJ*, 131, 168
- Lacey C., Cole S., 1994, *MNRAS*, 271, 676
- Maciejewski M., Colombi S., Springel V., Alard C., Bouchet F. R., 2009, *MNRAS*, 396, 1329
- Mathis H., Lemson G., Springel V., Kauffmann G., White S. D. M., Eldar A., Dekel A., 2002, *MNRAS*, 333, 739
- Merritt D., 1984, *ApJ*, 276, 26
- Mihos J. C., 2004, in *Mulchaey J. S., Dressler A., Oemler A., eds, Clusters of Galaxies: Probes of Cosmological Structure and Galaxy Evolution Interactions and Mergers of Cluster Galaxies*. pp 277+
- Mihos J. C., Harding P., Feldmeier J., Morrison H., 2005, *ApJ*, 631, L41
- Monaco P., Murante G., Borgani S., Fontanot F., 2006, *ApJ*, 652, L89
- Moore B., Katz N., Lake G., Dressler A., Oemler A., 1996, *Nature*, 379, 613
- Murante G., Arnaboldi M., Gerhard O., Borgani S., Cheng L. M., Diaferio A., Dolag K., Moscardini L., Tormen G., Tornatore L., Tozzi P., 2004, *ApJ*, 607, L83
- Murante G., Giovalli M., Gerhard O., Arnaboldi M., Borgani S., Dolag K., 2007, *MNRAS*, 377, 2
- Napolitano N. R., Pannella M., Arnaboldi M., Gerhard O., Aguerri J. A. L., Freeman K. C., Capaccioli M., Ghigna S., Governato F., Quinn T., Stadel J., 2003, *ApJ*, 594, 172
- Neyrinck M. C., Gnedin N. Y., Hamilton A. J. S., 2005, *MNRAS*, 356, 1222
- Rudick C. S., Mihos J. C., McBride C., 2006, *ApJ*, 648, 936
- Salpeter E. E., 1955, *ApJ*, 121, 161
- Saro A., Borgani S., Tornatore L., Dolag K., Murante G., Biviano A., Calura F., Charlot S., 2006, *MNRAS*, 373, 397
- Sommer-Larsen J., Romeo A. D., Portinari L., 2005, *MNRAS*, 357, 478
- Springel V., 2005, *MNRAS*, 364, 1105
- Springel V., Hernquist L., 2002, *MNRAS*, 333, 649
- Springel V., Hernquist L., 2003, *MNRAS*, 339, 289
- Springel V., White S. D. M., Tormen G., Kauffmann G., 2001, *MNRAS*, 328, 726
- Stadel J. G., 2001, *PhD thesis, AA(UNIVERSITY OF WASHINGTON)*
- Stanghellini L., González-García A. C., Manchado A., 2006, *ApJ*, 644, 843
- Tornatore L., Borgani S., Dolag K., Matteucci F., 2007, *MNRAS*, 382, 1050
- Tornatore L., Borgani S., Matteucci F., Recchi S., Tozzi P., 2004, *MNRAS*, 349, L19

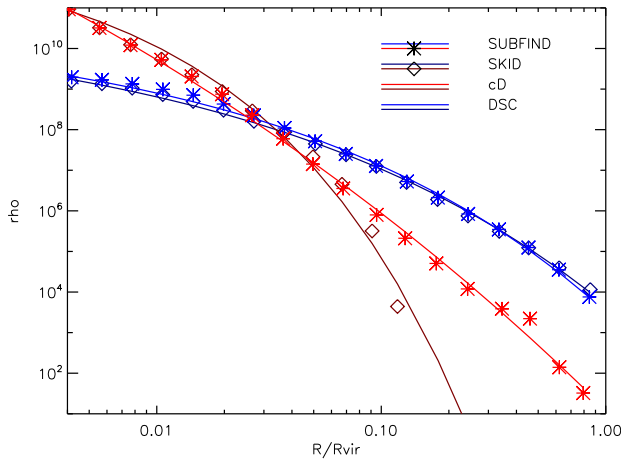


Figure A2. As in Figure 8, the stellar density profile of the *cD* (red symbols) and the *DSC* (blue symbols) are shown. The red and blue lines represent a Sersic fit to the distributions. Diamonds with solid lines and stars with dashed lines are the results obtained with SKID and SUBFIND respectively.

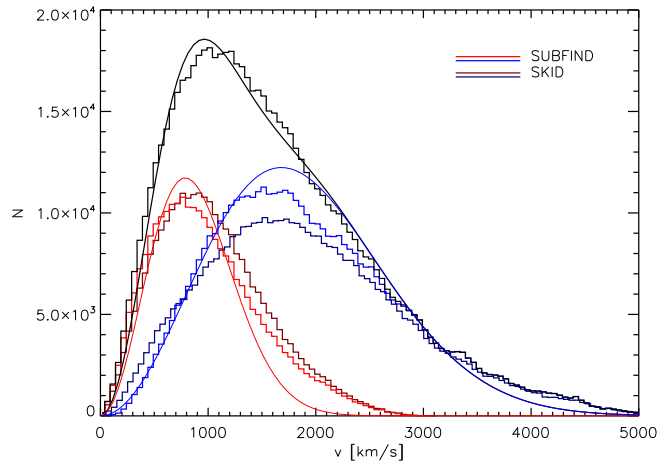


Figure A3. As in Figure 7, velocity histogram (black histogram) of the main halo stellar component and a double Maxwellian fit to it (thin line) is shown. Additionally, the red and blue histograms show the velocity distribution of the *cD* and *DSC* components and the thin lines indicate the individual, Maxwellian distributions obtained from the global fit. Light and dark colored histograms are the results obtained with SKID and SUBFIND respectively.

Weinberg D. H., Hernquist L., Katz N., 1997, *ApJ*, 477, 8
 Willman B., Governato F., Wadsley J., Quinn T., 2004, *MNRAS*, 355, 159
 Zibetti S., White S. D. M., Schneider D. P., Brinkmann J., 2005, *MNRAS*, 358, 949

APPENDIX A: SKID – SUBFIND COMPARISON

The identification of galaxies in M04 and M07 was based on a SKID. (Stadel 2001). For obtaining stable results, SKID parameters must be tuned carefully for correctly identifying individual galaxies. Namely, M07 showed that three different smoothing length

must be used, and the results of the three analysis combined, to avoid spurious loss of low density galaxies. Moreover, in SKID analysis, a typical scale length τ must be supplied for performing the un-binding procedure. Here (as in M04 and M07), we linked such a scale to the gravitational softening ϵ of the simulation: $\tau = 3\epsilon$. M07 showed that this choice is well suited to obtain a reasonable separation between the *cD* and the *DSC*.

The differences found between the SUBFIND and SKID for the *cD* vs. *DSC* separation as a function of mass, could be due to the fact that un-binding in clusters of different masses uses the same τ . In smaller clusters, more *DSC* particles could be improperly assigned to central galaxies. Such a problem is not present in our new SUBFIND scheme.

One additional small but systematic difference is in previous studies based on SKID where always based on all star particles within the virial radius, whereas SUBFIND operates on all particles belonging to a FoF group. The linking length is usually chosen to correspond to the virial over-density in a given cosmology and therefore the total mass or the amount of stars is quite similar in both analysis, but the FoF group usually is elliptically elongated and therefore the particles sets the two algorithms start from are not exactly the same in the outer region of the cluster.

A1 A detailed case study for a massive cluster

Here we compare the analysis of the high resolution simulation (e.g. the *3x* run) applying both methods to check the differences details when applying the two algorithm.

Figure A1 shows a direct comparison of all star particles in the different components as identified by SKID (left column) and SUBFIND (right column) within half of the virial radius of the cluster. It is quite encouraging that practically all galaxies have counterparts in both methods. In general, it seems that the un-binding applied by SUBFIND tend to unbind a little bit more the outer envelope of satellite galaxies, which in return appear as small over-densities in the *DSC* component. On the contrary, the *cD* identified by SUBFIND has smoother boundaries, while it looks more truncated in the SKID analysis. Nevertheless, the mass of the *cD* component is very similar, namely $1.28 \times 10^{13} M_{\odot}/h$ versus $1.21 \times 10^{13} M_{\odot}/h$ in SKID and SUBFIND respectively. Note that the *cD* velocity dispersion is similar in both analysis. SKID truncates the galaxy simply because its farther stars are not assigned to the *cD*, but to some satellite galaxy to which they don't belong, during SKID FoF phase. Then, they become unbound in the un-binding phase. SUBFIND assign such stars to the main sub-halo, and lately, they are *not* unbind from the *cD*.

The *DSC* looks extremely similar in both algorithms, which is also reflected in a quasi indistinguishable density profile as shown in figure A2. Here also the *cD* component shows excellent agreement in the inner part, again the differences in the outer parts are visible. We note that also in the outer parts the *DSC* components in both methods fall on top of each other, despite the previously discussed small differences in the underlying particle sets.

Figure A3 shows the velocity distribution in the two components. Already in the SKID analysis the difference in the dynamics of the two components are visible. Although again very similar, the SUBFIND results are more closely following the decomposition of the main stellar component into two Maxwellian distributions, as expected. Again, despite the different underlying algorithms, the total velocity distributions of all star particles used in SKID and SUBFIND is quasi indistinguishable and also leads to the same double Maxwellian fit. Therefore, we plotted in figure A3 only the total

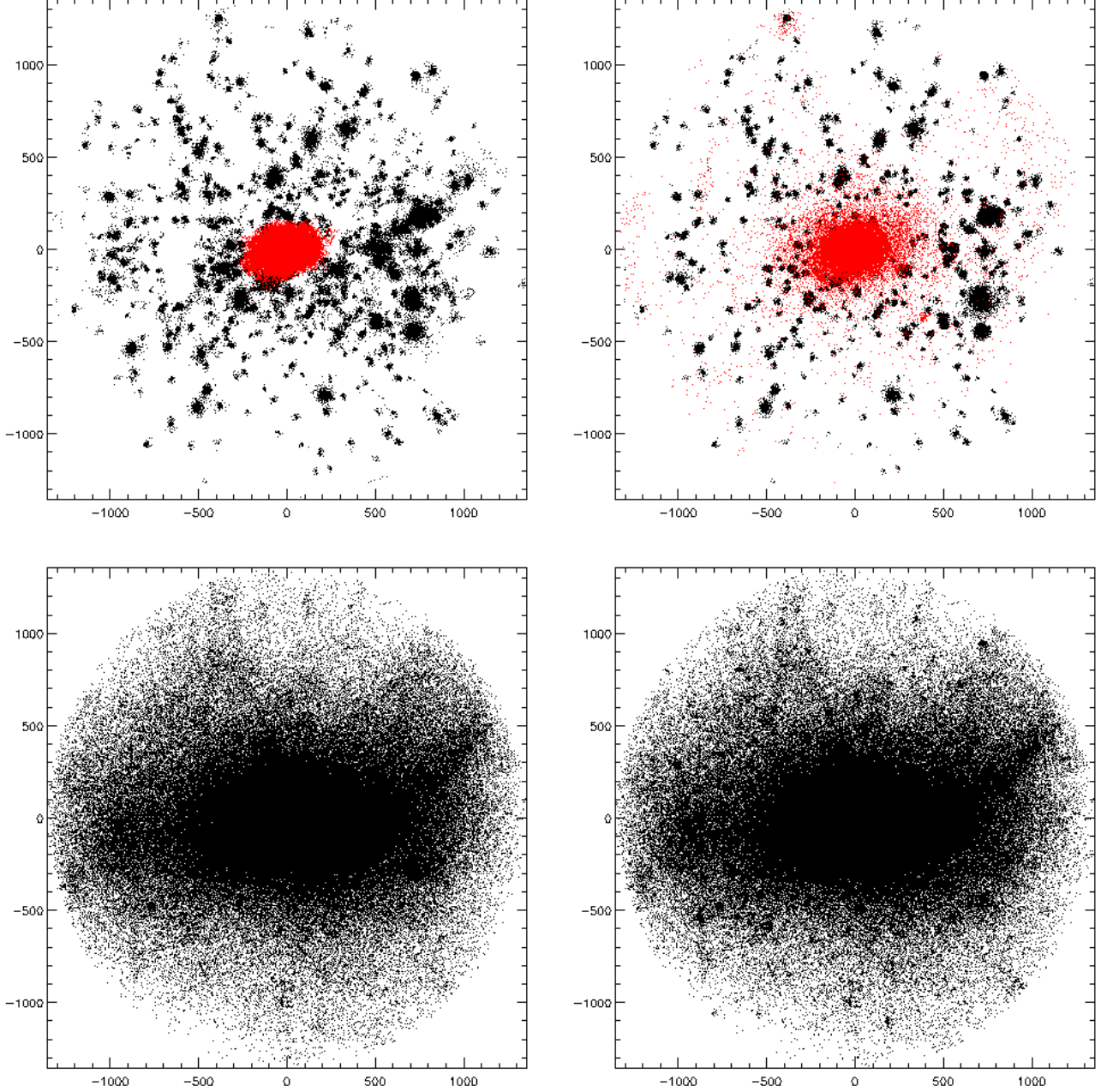


Figure A1. All star particles within $R_{vir}/2$ of the high resolution ($3x$) cluster belonging to individual galaxies (black dots in the upper row), the cD component (red dots in the upper row) and the DSC component (lower row). The left column is obtained applying SKID, the right column is our SUBFIND result.

distribution and the Maxwellian fits to SUBFIND data to avoid confusions.

A2 An example of a low mass cluster

Analyzing a smaller cluster ($M_{vir} \approx 2 \times 10^{14} M_{\odot}/h$) from our simulations reveals the differences between the two algorithms for such less massive systems. Although the individual satellite galaxies match as nicely as before, SKID assigns much more stars to the central cD than SUBFIND leading to the contrary behavior for the DSC component, which is clearly visible in figure A4, which, similarly to figure A1, shows a particle by particle comparison be-

tween the two algorithms. The differences in disentangling the cD and DSC component is also clear from figure A5, which shows the velocity distribution histograms of the inferred cD and DSC components. Whereas the SUBFIND results follow nicely, by construction, the individual components of the double Maxwellian fit to the global velocity distribution, the SKID results deviate significantly. In addition, we fitted individual Maxwellian distributions to the SKID results, shown as thin lines. It appears quite obvious that even such fits are not as good as the ones obtained with our new SUBFIND algorithm. Especially the cD component identified by SKID shows a significant tail towards higher velocities which can't be represented by a single Maxwellian distribution, indicat-

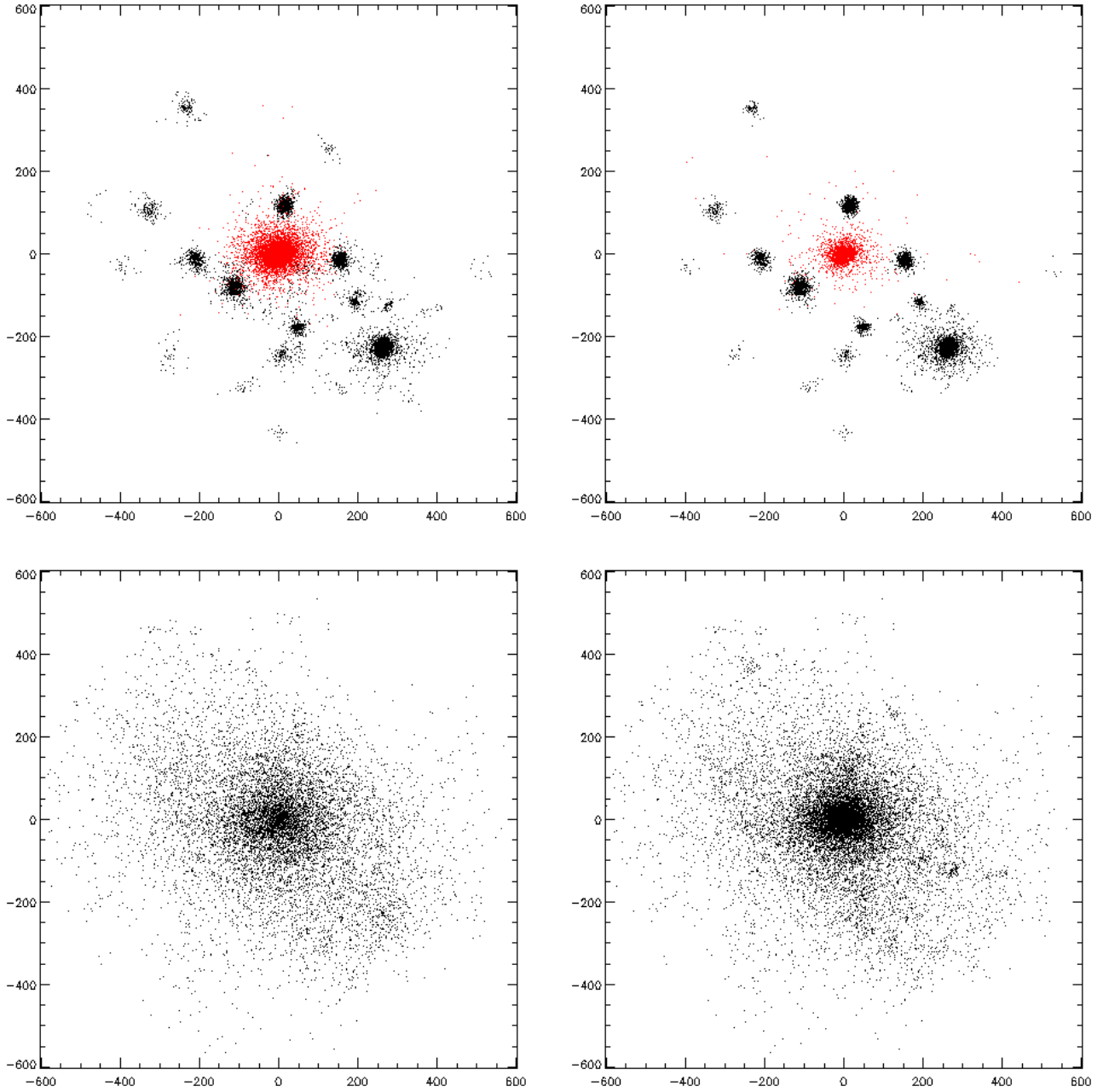


Figure A4. Same as figure A1, but for the small cluster where we found significant differences between the cD and DSC separation when applying SKID (left column) and SUBFIND (right column) respectively.

ing that the star particles associated to the cD by SKID are not a single, dynamical component.

To obtain better result with SKID, one should probably tune the τ parameter on a cluster-by-cluster basis. Such tuning is not needed with our new SUBFIND scheme.

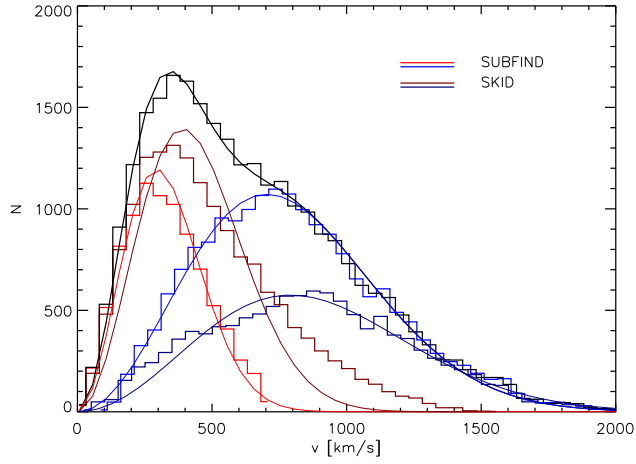


Figure A5. As in Figure A3, we show the velocity histogram (black) of the main halo stellar component and a double Maxwellian fit to it (thin line). Additionally, the red and blue histograms show the velocity distribution of the *cD* and *DSC* components and the thin lines indicate the individual, Maxwellian distributions obtained from the global fit. Light and dark colored histograms are the results obtained with SKID and SUBFIND respectively. The thin lines are individual Maxwellian fits to the *cD* and *DSC* components identified by SKID.